

See discussions, stats, and author profiles for this publication at: <https://www.researchgate.net/publication/263981648>

Theoretical Investigation of the Mechanism of the Water–Gas Shift Reaction on Cobalt@Gold Core–Shell Nanocluster

ARTICLE in THE JOURNAL OF PHYSICAL CHEMISTRY C · DECEMBER 2013

Impact Factor: 4.77 · DOI: 10.1021/jp408517m

CITATIONS

2

READS

41

6 AUTHORS, INCLUDING:



Hui-Lung Chen

Chinese Culture University

64 PUBLICATIONS 441 CITATIONS

SEE PROFILE



Feng-Yin Li

National Chung Hsing University

57 PUBLICATIONS 820 CITATIONS

SEE PROFILE

Theoretical Investigation of the Mechanism of the Water–Gas Shift Reaction on Cobalt@Gold Core–Shell Nanocluster

Sheng-Ke Wu,^{†,‡} Ren-Jie Lin,^{†,‡} Soonming Jang,[§] Hui-Lung Chen,^{||} Shih-Min Wang,[⊥] and Feng-Yin Li^{*,†}

[†]Department of Chemistry, National Chung Hsing University, Taichung 402, Taiwan

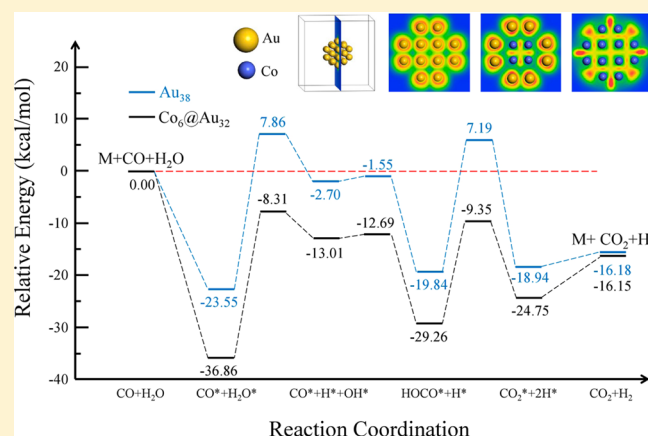
[§]Department of Applied Chemistry, Sejong University, Seoul 143-747, Korea

^{||}Department of Chemistry and Institute of Applied Chemistry, Chinese Culture University, Taipei 111, Taiwan

[⊥]Institute of Nuclear Energy Research, Lungtan, Taoyuan 325, Taiwan

S Supporting Information

ABSTRACT: We studied the mechanism of the water–gas shift reaction (WGSR; $\text{CO} + \text{H}_2\text{O} \rightarrow \text{CO}_2 + \text{H}_2$) catalyzed by $\text{Co}_6\text{@Au}_{32}$ core–shell nanoalloy using density-functional theory (DFT) calculations to investigate the bimetallic effects on the catalytic activation. The molecular structures and adsorbate/substrate interaction energies were predicted, along with the potential energy surface constructed using the nudged elastic band (NEB) method. Our results indicated that the energetic barriers of the two hydrogen dissociation reactions are lower on the core–shell nanoalloy than on Au_{38} . Furthermore, all of the related chemical species of the WGSR can adsorb stably on $\text{Co}_6\text{@Au}_{32}$ to allow the reactions to take place under ambient pressure. To gain insight into the synergistic effect in the catalytic activity of the $\text{Co}_6\text{@Au}_{32}$ nanoalloy, the nature of the interaction between the adsorbate and substrate was analyzed by detailed electronic local densities of states (LDOS) as well as molecular structures.



INTRODUCTION

Since Haruta et al.'s pioneering findings on the catalysis of CO oxidation with small gold nanoparticles,¹ the use of gold-based catalysts has become a topic of considerable interest mostly because of their potential usage in various industrial applications, such as carbon monoxide removal in hydrogen purification for polymer electrolyte fuel cells and some selective hydrogenation reactions in the synthesis of fine chemicals.^{2–10} To explore more active catalysts with superior performance and stability, considerable research^{11–21} has been devoted to gold-related bimetallic nanoparticles, which can provide more tunability than their single-metal counterparts because their properties depend not only on the composition but also on the atomic ordering. Furthermore, bringing one more metals together can lead to completely new phenomena, so-called synergistic effects,^{22,23} which have no counterpart in bulk materials or single-metal nanoparticles. However, these advantages simultaneously present a great challenge for actual implementation because there are so many possible potential conformer structures and each of them could exhibit certain unpredictable properties. Among the various types of bimetallic nanoparticles, core–shell structures have recently become one of the increasingly important systems because, with defined composition and structure, they can provide predictable control

over structural, geometric, and electronic effects on the catalytic properties; moreover, a generalized synthetic procedure was reported to create core–shell nanoparticles utilizing a redox transmetalation process.²⁴ The catalytic applications of core–shell bimetallic nanoparticles were reviewed recently by Jiang and Xu.²⁵ To evaluate the probable influence of a second metal in gold-based bimetallic nanoparticles, the water–gas shift reaction (WGSR) can serve as a good study system because this reaction has been studied extensively and its reaction mechanism is well-understood.^{26–28}

The WGSR, $\text{CO} + \text{H}_2\text{O} \rightarrow \text{CO}_2 + \text{H}_2$, is an important industrial reaction in providing high-purity hydrogen for fuel cells and numerous industrial applications.^{26–28} In addition, it is essential for any practical device that generates hydrogen from a hydrocarbon source. The interest in the WGSR has grown significantly because of its potential capability for the mass production of H_2 , as required by the hydrogen economy and fuel cell applications.^{29–35} Industrially, the WGSR is catalyzed by two different materials according to the operating temperature: FeCr-based catalysts for high temperature

Received: August 26, 2013

Revised: December 17, 2013

Published: December 17, 2013

(350–450 °C) and CuZn-based catalysts for low temperature (180–250 °C). However, in addition to requiring lengthy preactivation to prevent agglomeration of the metal, Cu-based catalysts are sensitive to condensed water and become pyrophoric if exposed to air.^{36,37} These features make Cu-based catalysts unsuitable for fuel cell applications. Therefore, a renewed search has been sparked for high-efficiency catalysts to improve the WGS rate that are also highly stable, especially operating at temperatures lower than 250 °C. Noble metals (e.g., Au and Pt) supported on ceria oxide carriers exhibit high catalytic activity for the low-temperature WGS without preactivation and are nonpyrophoric.^{37,38} The main reason for this high catalytic activity, as recently reviewed by Rodriguez,³⁹ is that the metal nanoparticle and the oxide support can work cooperatively to facilitate the different reaction steps: the adsorption and dissociation of water take place on the oxide, CO adsorption occurs on Au nanoparticles, and all subsequent reaction steps occur at oxide–metal interfaces. However, the detailed reaction mechanism of the WGS catalyzed by Au–ceria catalysts still remains unsettled.^{40,41} Two main alternatives have been proposed in the literature, namely, redox and associated mechanisms, where the latter can be further divided into formate and carboxyl mechanisms.⁴² In the redox mechanism, the CO adsorbed on the metal surface is oxidized by a labile oxygen atom of the support to form an oxygen vacancy site, and the oxygen vacancy site is then reoxidized by water, leading to the formation of a hydrogen molecule.^{43–47} According to the associated mechanism, the adsorbed CO reacts with terminal hydroxyl groups of the oxidic support to form carbon-containing intermediates, namely, formate and carboxyl, which further react or decompose to form CO₂ and H₂.^{48–50} Recently, using steady-state isotopic transient kinetic analysis (SSTIKA), Kalamaras et al. concluded that formate is mainly a spectator species.^{43,44} Therefore, the associated mechanisms are mainly through carboxyl pathway.

Although Au–ceria catalysts are particularly active and stable, their potential in fuel cell applications is severely hindered by their rapid deactivation due to the buildup of the adsorbed carbonate species on ceria surface, the irreversible over-reduction products generated by the ceria support.^{51,52} These carbonate species act as reaction-inhibiting spectators by either blocking the reaction active sites or preventing the reaction intermediates from accessing these active sites.^{52,53} Even though these carbonate species can be removed by annealing in O₂ environment at 400 °C to regain 95% of the initial activity on the fresh catalyst, the rapid deactivation makes the half-lives of Au–ceria catalysts too short for some fuel cell applications.⁵⁴

Recently, Au nanoparticles smaller than 1.4 nm supported on inert materials were reported to be efficient and robust catalysts for selective oxidation by O₂.¹⁰ Without help from the reducible support, the energetic barriers for hydrogen dissociation of the hydroxyl groups, an important reaction step in the redox mechanism, are rather high, and therefore, the lowest-energy pathway for the WGS over Au nanoparticles with an inert support is an associated mechanism through a carboxyl intermediate, as suggested by density-functional theory (DFT) studies.^{29,31} Previously, we showed that gold nanoparticle catalysts meet this purpose well with their high surface-to-volume ratios, which not only reduce the amount of catalytic material required but also enhance the catalytic activity compared with that of their bulk counterparts.⁵⁵ To further

reduce the usage of the precious metal and simultaneously increase the catalytic activity and stability of the catalysts, gold-based bimetallic nanoparticles² are promising candidates. For example, several experimental studies have demonstrated that gold-based bimetallic nanoparticles on different oxide supports can act as catalysts at lower temperature than regular catalysts or even below room temperature.^{11–21} However, there are few theoretical reports on the catalytic effects of bimetallic nanoparticles, and all of them focus on the CO oxidation reaction.^{56–58}

In this study, we applied periodic density-functional calculations to investigate the WGS process on the Co₆@Au₃₂ core–shell nanostructure. The reasons for choosing the Co₆@Au₃₂ core–shell nanostructure as a low-temperature WGS catalyst are the following: First, there are two main disadvantages of using Au₃₈ for the WGS, as found in our previous study.⁵⁵ For the WGS on Au₃₈, the transition states for two O–H bond dissociation reactions have adsorption energies larger than the total energy of the bare Au₃₈ and the gas-phase CO₂ and H₂O. This fact requires these reactions to be performed under high pressure to prevent the reactive complexes from flying away from the surface. Furthermore, the energetic barriers for these bond dissociation reactions on Au₃₈ are relatively high (31.41 and 27.03 kcal/mol), and any energy reduction in these two barriers should enhance the catalytic performance. As predicted by Huang et al. through a systematic reaction mechanism analysis among nine different transition-metal surfaces covering rows 3d–5d with groups 9 (Co, Rh, and Ir), 10 (Ni, Pd, and Pt), and 11 (Cu, Ag, and Au),⁵⁹ the Co metal surface has relatively low energetic barriers for O–H bond dissociation of water molecules and hydroxyl radicals but a rather high barrier for C–O bond formation, whereas the Au metal surface shows the opposite trend, that is, it has a high barrier for O–H bond dissociation and a low barrier for C–O bond formation. Because the Cu metal surface has mild barriers in both O–H bond dissociation and C–O bond formation, it makes the Cu surface have better catalytic activity than the Co and Au surfaces.⁵⁹ Furthermore, the Co surface has higher adsorption energies for both CO and H₂O than the Au surface.⁵⁹ We surmised that, with the synergetic effects of the combination of Co and Au metals on the WGS, Co₆@Au₃₂ core–shell nanoparticles might overcome these disadvantages. Second, Co@Au core–shell nanoparticles have been synthesized and characterized successfully by several research groups.^{24,60–62} So far, the research on Co@Au core–shell nanoparticles has mainly focused on the potential application of their magnetic and optical properties, along with their synthesis and characterization methods.^{31,61,63} To the best of our knowledge, this study is the first regarding the catalytic activity of Co@Au core–shell nanoparticles on the WGS. The closest related study is perhaps that of Venugopal et al.,¹¹ who compared the WGS activity catalyzed by a Co–Au nanoalloy against those of a series of Au-based bimetallic nanoclusters, but these nanoclusters were not core–shell structures because their synthesis method was the deposition coprecipitation method. Other core–shell bimetallic catalysts related to Co@Au nanoparticles have been investigated, for example, Ag@Au for glucose oxidation,⁶⁴ Pd@Au for the oxidation of alcohols,⁶⁵ and Co@Pt for the dehydrogenation of aqueous NH₃BH₃.⁶⁶ Finally, Co nanoparticles smaller than 4.4 nm are subject to water-induced oxidation to become cobalt oxides because of their surface free energies, but this type of oxidation will not take place on the bulk Co surface.^{67–69} Therefore, we excluded

Co nanoparticles from the energetic calculations because of their instability in water environments. Furthermore, as reported by Ban et al.,⁷⁰ Co@Au core-shell nanoparticles are stable in water and under acidic conditions because of the protection of the Au shell. The operating cost and reactivity of the WGSR can be significantly improved if the core Co atoms enhance the adsorption stability of CO and H₂O and, at the same time, the surface Au atoms catalyze the reactions enhanced by the core Co atoms. We believe that this study is vital for understanding the factors governing the WGSR catalyzed synergistically by nanosized gold bimetallic clusters.

COMPUTATIONAL METHODS

All of the reaction species of the WGSR, including reactants, intermediates, transition states, and products, as well as the nanoparticles, were calculated using spin-polarized density-functional theory (DFT)⁷¹ with a plane-wave basis set, as implemented in the Vienna ab initio simulation package (VASP) program.^{71–76} The generalized gradient approximation (GGA)⁷⁷ with the PW91 functional⁷⁸ was employed in conjunction with the projector augmented wave (PAW) potential to describe the interaction between core and valence electrons. The open-shell spin states of the radical intermediates, such as OH and H radicals, were set as ISPIN = 2 in the calculations. For the supercell, we chose a cube size of 25³ Å³, which is large enough to ensure that the integration of nanoparticles with their images is negligible. A 400 eV cutoff energy, which was adequate for convergence to a total energy of 1×10^{-4} eV, was used together with the Γ point for the summation in the Brillouin zone. In this work, we calculated the adsorption energies according to the expression

$$\Delta E_{\text{ads}} = E_{\text{total}} - E_{\text{Co}_6\text{@Au}_{32}} - E_{\text{adsorbate}} \quad (1)$$

where E_{total} , $E_{\text{Co}_6\text{@Au}_{32}}$, and $E_{\text{adsorbate}}$ correspond to the electronic energies of the adsorbed species on the Co₆@Au₃₂ nanoparticle, the bare Co₆@Au₃₂ nanoparticle, and a free adsorbate, respectively. Furthermore, the coadsorption energies of CO with H₂O molecule were calculated as

$$\Delta E_{\text{coads}} = E_{\text{total}} - E_{\text{Co}_6\text{@Au}_{32}} - E_{\text{CO}} - E_{\text{H}_2\text{O}} \quad (2)$$

The nudged elastic band (NEB) method^{79,80} was applied to construct the minimum-energy paths (MEPs) by connecting reactants, intermediates, transition states, and products. All chemical species were verified by the vibrational frequencies of the adsorbed structures, which were analyzed by diagonalizing the Hessian matrix of selected atoms within the VASP approach. Atomic charges of the selected structures were calculated by utilizing Bader charge^{81,82} analysis with a program designed by Henkelman et al.⁸³

To calculate the rate constants, we employed harmonic transition state theory (hTST)⁸⁴

$$k = \nu^* \exp\left(-\frac{E_a}{k_B T}\right) \quad (3)$$

where E_a is the activation energy, k_B is the Boltzmann constant, T is the temperature in Kelvin, and

$$\nu^* = \frac{k_B T}{h} \frac{\prod_{i=1}^D \left[1 - \exp\left(-\frac{\hbar \omega_i^R}{k_B T}\right)\right]}{\prod_{i=1}^D \left[1 - \exp\left(-\frac{\hbar \omega_i^S}{k_B T}\right)\right]} \quad (4)$$

is the quantum mechanically modified form of the prefactors, where D , ω_i^R , and ω_i^S are the number of normal modes and the nonimaginary vibrational frequencies of the i th mode in the reactants and saddle-point states, respectively.

RESULTS AND DISCUSSION

Comparison between Co₆@Au₃₂ and Au₃₈ Nanoparticles. Similarly to Au₃₈,⁸⁵ the Co₆@Au₃₂ nanoparticle is modeled as an tetrakaidecahedral structure with O_h symmetry within a 0.1-Å tolerance through structural optimization. As shown in Figure 1, there are eight equivalent hexagonal

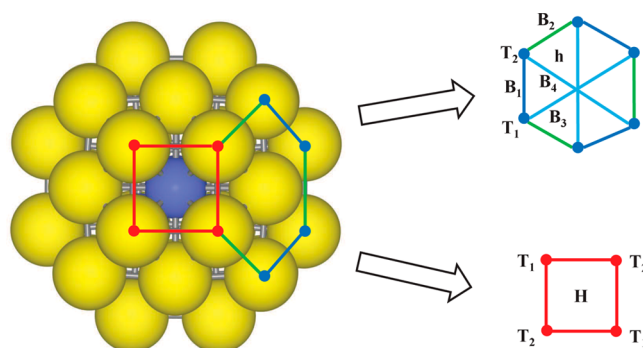


Figure 1. Schematic presentation of a Co₆@Au₃₂ nanoparticle. High-symmetry adsorption sites on a hexagonal face of the Co₆@Au₃₂ nanoparticle. T₁ and T₂ represent the top sites, B₁–B₄ represent the bridge sites, H represents the hole site, and h represents the hcp site.

fcc(111)-like faces and six equivalent square fcc(100)-like faces, similar to those found in the Au₃₈ cluster, characterized as top (T), bridge (B), hollow (H), and hexagonal-close-packed (hcp) sites. However, because the radius of the Au atom is slightly larger than that of the Co atom, the nanoparticles with cobalt atoms as the shell layer require more than 32 atoms to form stable structures. This is why gold–cobalt core-shell nanoparticles are not included in this study. Several characteristic differences between Co₆@Au₃₂ and Au₃₈ nanoparticles, such as geometry, structure, and adsorption information, are listed in Table 1, along with their charge information. For example, the calculated average nearest-neighbor bond distance between the shell gold atoms is 2.74 Å, and that between the core cobalt atoms is 2.42 Å. These two distances are slightly shorter than those of their single-metal counterparts as reported in the literature (2.78 Å for Au₃₈ nanoparticles⁷⁹ and 2.50 Å for Co₃₈ nanoparticles⁸⁶). However, the average bond distance between a shell gold atom and a core cobalt atom is 2.93 Å, slightly larger than the distance between their counterparts in Au₃₈ nanoparticles (2.83 Å). This Co–Co distance shrinkage in Co@Au nanoparticles was also found by Wang et al.⁸⁷ They attributed this shrinkage to the decrease of the total magnetic moment compared with that found in bare Co nanoparticle due to the antiparallel ordering of the spin moments of the shell Au atoms with respect to the spin moments of the Co core atoms.⁸⁷ The distance shrinkage between the shell Au atoms is because the size of the Co core is smaller than that of the Au core in Au₃₈ nanoparticles, making the shell Au atoms move slightly toward the center of the core-shell nanoparticles. This is why the size and surface area of a Co₆@Au₃₂ nanoparticle are slightly smaller than those of a Au₃₈ nanoparticle. However, the size shrinkage of the Co core is slightly more than the inward movement of the Au shell, which is why the average bond

Table 1. Geometrical and Structural Comparison between $\text{Co}_6@ \text{Au}_{32}$ and Au_{38} Nanoparticles, along with Their Adsorption Information with CO and H_2O Adsorbed onto Their Surfaces

	Au_{38}	$\text{Co}_6@ \text{Au}_{32}$
volume (\AA^3)	256.70	239.42
area (\AA^2)	20.79 (8.04) ^a	20.06 (7.51)
$d_{\text{shell-shell}}$ (\AA)	2.80	2.74
$d_{\text{core-core}}$ (\AA)	2.80	2.42
$d_{\text{core-shell}}$ (\AA)	2.83	2.93
charge on the shell (e)	−0.380	−2.146
charge on the core (e)	0.380	2.146
$d_{\text{H}_2\text{O}}$ (\AA)	0.97/0.97 ^b	0.97/0.98
$d_{\text{Au-O}}$ (\AA)	2.56 ^c	2.72
$E_{\text{ads}}(\text{H}_2\text{O})$ (kcal mol ^{−1})	−6.38 ^d	−4.04
d_{CO} (\AA)	1.17 ^e	1.17
$d_{\text{Au-C}}$ (\AA)	2.14/2.14 ^f	2.12/2.13
$E_{\text{ads}}(\text{CO})$ (kcal mol ^{−1})	−20.15 ^g	−31.81

^aArea of hexagon (area of square). ^bTwo O–H bond lengths of one H_2O adsorbed on a T_2 site. ^cDistance between the oxygen atom of the adsorbed H_2O and the gold atom of a T_2 site. ^dAdsorption energy of one H_2O adsorbed on a T_2 site. ^eC–O bond length of one CO adsorbed on a B_2 bridge site. ^fDistance between the carbon atom of the adsorbed CO and the two gold atoms of a B_2 site. ^gAdsorption energy of one CO adsorbed on a B_2 site.

distance between a shell gold atom and a core cobalt atom is slightly larger than the distance between their counterparts in Au_{38} nanoparticles.

Because the work function⁸⁸ of pure Co metal (5 eV) is slightly smaller than that of pure gold metal (5.10–5.47 eV), a negative charge distribution is built up in the shell gold atoms. This charge separation along with the area shrinking consequently influences the adsorption behavior of H_2O and CO molecules on the surface of this bimetallic nanoparticle. For example, the distance between the oxygen atom of H_2O and its adsorbed gold atom of a $\text{Co}_6@ \text{Au}_{32}$ nanoparticle is 2.72 \AA , slightly larger than that found in a Au_{38} nanoparticle (2.56 \AA). The adsorption energy of CO on a B_1 bridge site of $\text{Co}_6@ \text{Au}_{32}$ nanoparticle is $-31.81 \text{ kcal mol}^{-1}$, significantly different from that found on a B_1 site of a Au_{38} nanoparticle ($-20.15 \text{ kcal mol}^{-1}$).

Adsorption of CO, H_2O , OH, and H on a $\text{Co}_6@ \text{Au}_{32}$ Nanoparticle. Understanding the adsorption structures and related energetics of the WGS intermediate is significant for exploring the WGS process on the nanoparticle surface. To locate the probable stable adsorption configurations of WGS intermediates, such as $\text{Co}_6@ \text{Au}_{32}\text{--CO}$, $\text{Co}_6@ \text{Au}_{32}\text{--OH}$, $\text{Co}_6@$

$\text{Au}_{32}\text{--H}_2\text{O}$, and $\text{Co}_6@ \text{Au}_{32}\text{--H}$, we placed CO, OH, H_2O , and H species, respectively, at those sites on the surface of a $\text{Co}_6@ \text{Au}_{32}$ nanoparticle, as shown in Figures S1–S4, respectively, of the Supporting Information, and the corresponding adsorption energies of these isomeric adsorption structures are listed in Table 2. For CO adsorption, the molecule can adsorb on the $\text{Co}_6@ \text{Au}_{32}$ nanoparticle in various isomeric structures (Figure S1, Supporting Information), all with the “end-on” configuration, that is, using the C atom to bind to one of the shell Au atoms. Among all of the calculated CO adsorption structures on the $\text{Co}_6@ \text{Au}_{32}$ surface, only the adsorption energy of OC--B_1 (-31.18 kcal/mol) was larger than that found on the Au_{38} surface (-20.15 kcal/mol), and the adsorption energies for the rest of adsorption configurations were all smaller than their counterparts on the Au_{38} surface. Compared with their counterparts on the Au_{38} surface, the most stable CO adsorption structures were found to be OC--T_2 and OC--B_1 in the same end-on configuration, with smaller adsorption energies as -20.09 and -20.15 kcal/mol , respectively. A similar pattern was also found in the OH radical adsorption configurations (Figure S2, Supporting Information); that is, only the adsorption energy of OH--B_1 (-77.34 kcal/mol) was larger than that found on the Au_{38} surface (-66.41 kcal/mol), and the adsorption energies for the rest of the adsorption configurations were all smaller than their counterparts on the Au_{38} surface. Interestingly, the most stable adsorption configuration of $\text{Co}_6@ \text{Au}_{32}\text{--HO}$ is the HO--B_1 configuration, but the most stable adsorption configuration of $\text{Au}_{38}\text{--HO}$ is the HO--B_2 configuration. For $\text{Co}_6@ \text{Au}_{32}\text{--H}_2\text{O}$ adsorption (Figure S3, Supporting Information), the adsorption energies for all structures found in this study ranged from -0.88 to -6.07 kcal/mol , slightly smaller than their specific counterparts on the Au_{38} surface. Interestingly, the $\text{H}_2\text{O--T}_2$ configuration, with the oxygen atom adsorbed on a T_2 site of $\text{Co}_6@ \text{Au}_{32}\text{--H}_2\text{O}$, was found to be energetically the most stable among all of the adsorption structures, but for the $\text{Au}_{38}\text{--H}_2\text{O}$ adsorption structures, the most stable configuration was the $\text{H}_2\text{O--T}_1$ configuration. However, the results were quite different for the adsorption of the hydrogen atom because all of the adsorption configurations on the $\text{Co}_6@ \text{Au}_{32}$ surface (Figure S4, Supporting Information), except the H--B_2 configuration, were more stable than their specific counterparts on the Au_{38} surface. Obviously, the main reason for these differences is the influence of the core Co atoms, but the role played by these Co atoms is rather subtle because there is no direct interaction between the adsorbate and the core Co atoms. Most likely, these core Co atoms exert their influence first by changing the properties of the shell Au atoms and then the shell Au atoms interact with

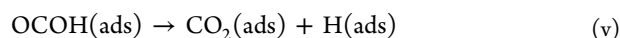
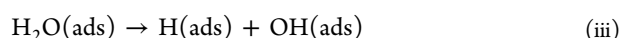
Table 2. Calculated Adsorption Energies (kcal/mol) of Adsorbed CO, H_2O , OH, and H Species on Various Sites of a $\text{Co}_6@ \text{Au}_{32}$ Nanoparticle

site	CO	H_2O	OH	H
T_1	−17.14 (−17.16) ^a	−4.04 (−6.38)	−64.39 (NA ^b)	−65.51 (−57.24) ^a
T_2	−17.66 (−20.09)	−5.14 (−6.24)	−57.10 (−63.51)	−64.05 (−57.24)
B_1	−31.81 (−20.15)	−2.63 (−3.42)	−77.34 (−66.41)	−65.19 (−55.17)
B_2	−14.79 (−18.24)	−3.12 (−6.09)	−64.48 (−72.06)	−53.04 (−56.69)
B_3	−10.89 (−17.93)	NA	NA (−61.57)	NA (−56.87)
B_4	−8.53 (−17.92)	NA	NA (−61.83)	NA (−56.69)
H	−3.11 (−20.09)	−0.75 (−1.64)	−53.93 (−62.82)	NA
hcp	NA	NA	NA (−65.17)	NA (−54.53)

^aValues in parentheses are results on Au_{38} . ^bNot available

the adsorbates. To resolve the above phenomena, we investigated the effects of the core Co atoms on the WGSR through analysis of their electronic properties, such as the electronic local density of states (LDOS), in addition to the geometric and charge differences listed in Table 1. Before performing LDOS analysis, we investigated the probable reaction profile for the WGSR on the $\text{Co}_6\text{@Au}_{32}$ surface. In this way, we focused on only the critical conformations of the chemical species on the $\text{Co}_6\text{@Au}_{32}$ surface without going through all possible conformations.

Reaction Profile for WGSR on a $\text{Co}_6\text{@Au}_{32}$ Nanoparticle. The generally accepted reaction mechanism with the minimum energy barriers for the WGSR is the associative mechanism,^{89,90} which involves the following steps



where S represents the nanoparticle. We also tested the two main reactions related to the redox mechanism, $\text{OH(ads)} \rightarrow \text{H(ads)} + \text{O(ads)}$ and $\text{OH(ads)} + \text{OH(ads)} \rightarrow \text{H}_2\text{O(ads)} + \text{O(ads)}$, and found their energetic barriers to be 33.34 and 57.43 kcal/mol, respectively (Figure S6, Supporting Information), higher than the barrier of reaction v in the associative mechanism on Au_{32} . Therefore, we focused on only the associative mechanism, particularly the hydroxyl pathway.

Based on our adsorption results, we constructed the potential energy surface (PES) for the WGSR on a $\text{Co}_6\text{@Au}_{32}$ nanoparticle according to the above mechanism, as depicted in Figure 2. The important geometric illustrations of the intermediates, transition states, and products along the WGSR PES are presented in Figure S5 (Supporting Information), and the adsorption sites of these chemical species on a $\text{Co}_6\text{@Au}_{32}$

nanoparticle are summarized in Table S1 (Supporting Information), along with the corresponding sites for a Au_{38} nanoparticle. At first, CO and H_2O are coadsorbed to form **IM1** on the nanoparticle, where CO adsorbs on a B_1 site and H_2O adsorbs on a T_2 site for both nanoparticles. The coadsorption energy was calculated to be -36.86 kcal/mol on the $\text{Co}_6\text{@Au}_{32}$ surface, lower than that found on the Au_{38} surface (-23.55 kcal/mol), and the coadsorption energy was roughly the same as the sum of the corresponding adsorption energies of CO(ads) and $\text{H}_2\text{O(ads)}$ individually for $\text{Co}_6\text{@Au}_{32}$ (-36.95 kcal/mol) but slightly larger than that found on Au_{38} (-26.58 kcal/mol). For **IM1** of a $\text{Co}_6\text{@Au}_{32}$ nanoparticle, the distance between the O atom of H_2O and Au is 2.587 \AA , but this distance for a Au_{38} nanoparticle is 2.652 \AA . Although H_2O is closer to the gold atoms in a $\text{Co}_6\text{@Au}_{32}$ nanoparticle than in a Au_{38} nanoparticle, there is only small charge transfer between them according to the Bader charge analysis (Table 3). H_2O dissociation from **IM1** into adsorbed OH and H producing **IM2** for a $\text{Co}_6\text{@Au}_{32}$ nanoparticle requires an energetic barrier of 28.55 kcal/mol (**TS1**) with an endothermicity of 23.85 kcal/mol, but the corresponding barrier and reaction heat for a Au_{38} nanoparticle are 31.41 and 20.85 kcal/mol, respectively. Compared to Cu-related materials in terms of the reaction barrier of the water dissociation reaction, a $\text{Co}_6\text{@Au}_{32}$ nanoparticle is more reactive than a Cu(111) surface (31.36 kcal/mol) but still less reactive than a Cu(100) surface (26.06 kcal/mol) or a Cu_{29} nanoparticle (21.44 kcal/mol).^{29,31,91} In the structure of **TS1** for a $\text{Co}_6\text{@Au}_{32}$ nanoparticle, H_2O moves to an hcp site with one of the two hydrogen atoms pointing toward a B_2 site and the associated OH bond stretching from 0.98 to 1.26 \AA ; however, in the **TS1** structure for a Au_{38} nanoparticle, H_2O remains on a T_2 site, and the leaving hydrogen atom points toward a B_2 site, with the to-be-broken OH bond extended from 1.00 to 1.35 \AA . This indicates that a $\text{Co}_6\text{@Au}_{32}$ nanoparticle can stabilize the WGSR-related species more than a Au_{38} nanoparticle. Interestingly, OH(ads) of **IM2** for a $\text{Co}_6\text{@Au}_{32}$ nanoparticle moves from an hcp site to a T_2 site to react with CO(ads) and produce an OCOH(ads) species by passing through **TS2** with a low energy barrier of 0.32 kcal/mol and an exothermicity of 16.25 kcal/mol; the corresponding energy barrier and reaction heat for a Au_{38} nanoparticle are 1.15 and -17.14 kcal/mol, respectively. In **TS2** for a $\text{Co}_6\text{@Au}_{32}$ nanoparticle, the distance between the hydroxyl oxygen atom and the original T_2 -site gold atom of **IM1** is 4.11 \AA , and the forming C–O bond is 1.85 \AA ; at the same time, for a Au_{38} nanoparticle, the corresponding distance and C–O bond length are 2.53 and 1.89 \AA , respectively. The final decomposition of OCOH(ads) occurs by OH bond cleavage to produce $\text{CO}_2\text{(ads)}$ and H(ads) on T_1 and B_2 sites, respectively, for both nanoparticles. For a $\text{Co}_6\text{@Au}_{32}$ nanoparticle, this process requires a barrier of 19.91 kcal/mol with an endothermicity of 4.51 kcal/mol, but for a Au_{38} nanoparticle, it needs 27.03 kcal/mol to overcome the corresponding barrier with an endothermicity of 0.90 kcal/mol. The broken H–O bond of **TS3** was calculated to be 1.24 and 1.37 \AA for $\text{Co}_6\text{@Au}_{32}$ and Au_{38} nanoparticles, respectively. The adsorption energy of CO_2 was found to be 0.01 kcal/mol for a $\text{Co}_6\text{@Au}_{32}$ nanoparticle and -0.92 kcal/mol for a Au_{38} nanoparticle, suggesting that the CO_2 molecule is only physisorbed on both nanoparticles. Before H_2 desorption from a $\text{Co}_6\text{@Au}_{32}$ nanoparticle, the two adsorbed hydrogen atoms that are generated in reaction iii on a B_1 site and in reaction v on a B_2 site, with the sum of their adsorption energies being 5.69 kcal/mol, recombine to form

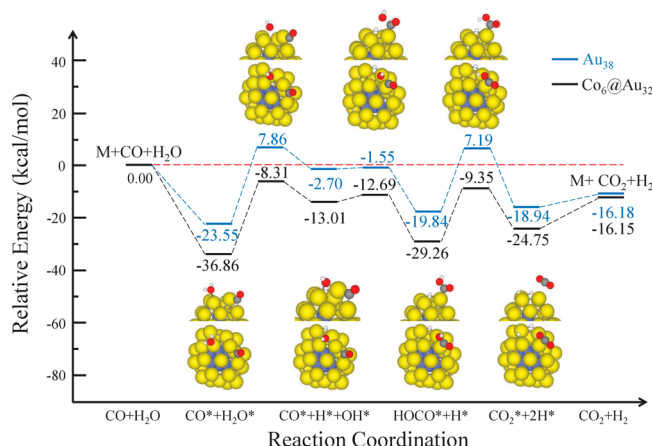


Figure 2. Calculated probable potential energy diagram for the reaction of H_2O and CO on both the $\text{Co}_6\text{@Au}_{32}$ and Au_{38} nanoparticles, where the numbers are the energies related to the reactants in kcal/mol.

Table 3. Bader Charges of Metal Atoms; C and O1 of CO; and H1, H2, and O2 of H₂O for the Stationary States along the Minimum-Energy Pathway of the WGS Reaction on a Co₆@Au₃₂ Nanoparticle

	H ₂ O, CO, Co ₆ @Au ₃₂	OC–Co ₆ @Au ₃₂	H ₂ O–Co ₆ @Au ₃₂	IM1	IM2	IM3	IM4
C	1.844	1.705 (1.707)		1.734 (1.737)	1.763 (1.836)	2.608 (2.489)	4.000 (4.000)
O1	–1.844	–1.913 (–1.960)		–1.942 (–1.942)	–1.918 (–1.968)	–1.910 (–1.881)	–2.011 (–2.028)
O2	–1.999		–1.962 (–1.969)	–1.950 (–1.969)	–1.469 (–1.470)	–1.928 (–1.891)	–2.014 (–2.003)
H1	1.000		1.000 (1.000)	0.999 (1.000)	–0.098 (–0.089)	–0.108 (–0.109)	–0.118 (–0.150)
H2	1.000		1.000 (1.000)	1.000 (1.000)	1.000 (1.000)	1.000 (1.000)	–0.115 (–0.076)
Au(C1)	–0.065 (–0.010)	0.050 (0.082)		0.026 (0.068)	–0.001 (0.059)	–0.022 (0.139)	–0.015 (–0.056)
Au(C2)	–0.066 (–0.006)	0.055 (0.072)		0.074 (0.068)	0.369 (0.030)	0.080 (–0.008)	–0.007 (–0.033)
Au(O2)	–0.013 (–0.025)		–0.048 (0.0455)	0.020 (0.030)	0.103 (0.257)	–0.026 (0.025)	0.034 (0.030)
Co(Au1,Au2)	0.377	0.370		0.369	0.379	0.381	0.374
Co(Au3)	0.334		0.344	0.336	0.318	0.314	0.319

^aO1 represents the O atom of CO, O2 represents the O atom of H₂O, H1 represents the first dissociated hydrogen atom of H₂O, and H2 represents the second one. Values in parentheses are those corresponding to a Au₃₈ nanoparticle. ^bAu(C1), Au(C2), and Au(O2) represent the Au atom bonding with the C atom of CO and the O atom of H₂O, respectively, whereas Co(Au1,Au2) and Co(Au3) represent the nearest Co atoms to Au(C1,C2) and Au(O2), respectively.

H₂(ads) on a T₁ site. The adsorption energy of H₂(ads) is 9.51 kcal/mol, implying that H₂(ads) can desorb from the Co₆@Au₃₂ nanoparticle surface to become H₂(g) at room temperature.

According to the reaction profile on a Co₆@Au₃₂ nanoparticle, the relative energies of all of the WGS-related chemical species are less than 0 compared with the energies of the free adsorbates and clear Co₆@Au₃₂ nanoparticle; therefore, the reaction should be able take place without a high-pressure environment. On the other hand, for the reactions on a Au₃₈ nanoparticle, the relative energies of TS1 and TS3 are slightly greater than 0. Moreover, the three energy barriers of the WGS on a Co₆@Au₃₂ nanoparticle are lower than those found on a Au₃₈ nanoparticle (2.86, 0.83, and 7.12 kcal/mol lower for reactions iii–v, respectively). Thus, a Co₆@Au₃₂ nanoparticle is more reactive than a Au₃₈ nanoparticle, which was predicted to exhibit better performance than various copper and gold surfaces, as shown in our previous work.⁵⁵ We calculated the rate constant of the rate-limiting step [H₂O(ads) → H(ads) + OH(ads)] with the quantum-mechanical modified hTST and found that hydrogen dissociation of a water molecule can take place with rate constants ranging from 6.78 × 10^{–2} to 0.495 s^{–1} within the WGS low-temperature range (180–250 °C) and from 1.26 × 10² to 1.09 × 10³ s^{–1} for the WGS high-temperature range (350–450 °C).

Interestingly, the activation energies and reaction heats (both in kcal/mol) for reactions iii–v on Co₆@Au₃₂ are (28.55, 23.85), (0.32, –16.25), and (19.19, 4.51), respectively, whereas the corresponding values on Au₃₈ are (31.41, 20.85), (1.15, –17.14), and (27.03, 0.90), respectively. The activation energies of these three reactions on Co₆@Au₃₂ are lower than the corresponding ones on Au₃₈, but all of the reaction heats on Co₆@Au₃₂ are more endothermic than the corresponding values on Au₃₈. However, these observations seem to contradict the prediction of the general Brønsted–Evans–Polanyi (BEP) relation,^{92–97} a linear relationship between the transition state energy and reaction energy of a reaction. To resolve this issue, we resorted to the molecular and electronic structures along the reaction pathway. Before doing that, we investigated the LDOS of the related nanoparticles in this study to provide general information about the electronic structures to facilitate the discussion.

Analysis of the Electronic State of the Nanoparticles.

To understand the bimetallic effect, we calculated the LDOS of pure and core–shell nanoparticles as shown in Figure 3. The d-band centers for Au₃₈, Co₆@Au₃₂, and Co₃₈ were found to be –3.495, –3.188, and –2.329 eV, respectively. According to the d-band model of chemisorption developed by Hammer and Nørskov,⁹⁸ the metal surface with its d-band center close to the Fermi energy tends to produce a strong interaction between the metal surface and the adsorbed molecule. This partially explains why the relative energies of all of the WGS-related chemical species on Co₆@Au₃₂ are more stable than their counterparts on Au₃₈. In addition, the d-band distribution of Co₆@Au₃₂ around the Fermi energy is similar to that of Au₃₈ because both of them have an energy gap (~1.0 eV) between the bands around the Fermi energy, although this energy gap for Co₃₈ is less than 0.1 eV, if only the d bands are considered. This indicates that the reactivity of Co₆@Au₃₂ should be similar to that of Au₃₈ and is quite different from that of Co₃₈. This energy gap found in Co₆@Au₃₂ is strongly influenced by the d-band distribution of the core Co atoms. For example, the upward shifting in the two d bands of Au₃₈ (around –1 and 0

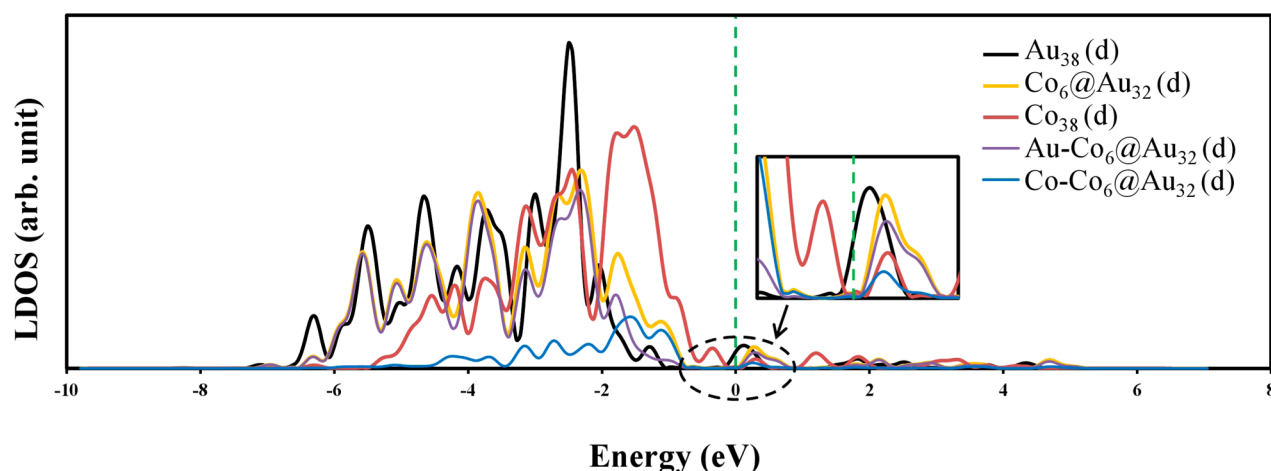


Figure 3. Local densities of states (LDOS) of Au_{38} , $\text{Co}_6@Au_{32}$, and Co_{38} nanoparticles along with the contributions from the shell Au atoms and core Co atoms in $\text{Co}_6@Au_{32}$. The green dashed line represents the Fermi level.

eV) and the downward shifting in the d bands of Co_{38} below the Fermi energy match with the corresponding d bands of the core Co atoms. However, the d band of $\text{Co}_6@Au_{32}$ just above the Fermi energy remains almost the same as those of Co_{38} , except that there is a shoulder band around 0.8 eV, which is not found in either Co_{38} or Au_{38} , contributed exclusively from the shell Au atoms of $\text{Co}_6@Au_{32}$. The main reason for the above observation is the hybridization between the high-lying occupied d bands of the core Co atoms and the unoccupied d bands just above the Fermi energy in the shell Au atoms. Because of this hybridization, those high-lying occupied d bands of the core Co atoms shift downward, and those unoccupied bands of the shell Au atoms near the Fermi energy shift upward with a shoulder band. Similarly, the reverse of the above interaction, that is, the occupied Au d bands and unoccupied Co d bands near the Fermi energy, should take place. However, because of the small portion of the Au d band on the Fermi energy being occupied, only a small upward-shifted shell Au d band is found (approximately -1.0 eV), and almost no changes are found for the unoccupied Co d band (~ 0.2 eV). Hence, by summing the above two processes, d electrons are transferred from the core Co atoms to the shell Au atoms, as predicted by their work functions. This phenomenon can be easily observed through an electron localization function (ELF) analysis (Figure 4). The electron density distribution of $\text{Co}_6@Au_{32}$ can be divided into two parts,

the shell and the core. The shell electron density closely resembles the electron density of Au_{38} , but more electron density localizes on the shell Au atoms. The core electron density shares the pattern found in Co_{38} . The catalytic reactions, on the other hand, is mainly controlled by the shell Au atoms, and therefore, the WGS on $\text{Co}_6@Au_{32}$ is very similar to that found on Au_{38} , but the electron density of the shell Au atoms near the Fermi level was shifted upward due to the Co core atoms and enhanced the catalytic activity of $\text{Co}_6@Au_{32}$ without breaking the stability. Therefore, a better Au-based core-shell catalyst has the occupied Au d bands shifted upward toward the Fermi level to enhance its catalytic activity but preserves the d-band pattern of noble metals near the Fermi level to maintain the stability.

Comparison between $\text{Co}_6@Au_{32}$ and Au_{38} during the WGS. We applied detailed LDOS analyses to the adsorbed constructs of H_2O and CO species, as well as with the d-projected electron density of the bonded Au atoms and nearby Co atoms, as depicted in Figure 5, along the reaction pathway, where Figure 5a shows the LDOS of the isolated H_2O , CO, and $\text{Co}_6@Au_{32}$ nanoparticle and panels b–h of Figure 5 correspond to the LDOS of the IM1, TS1, IM2, TS2, IM3, TS3, and IM4 configurations, respectively. For comparison, a similar LDOS analysis of a Au_{38} nanoparticle is shown in Figure 6. In this section, we investigate the different behaviors in the electronic states between $\text{Co}_6@Au_{32}$ and Au_{38} nanoparticles along the WGS reaction pathway to resolve the energetic issue regarding the BEP relationship as found in the previous section, combined with the corresponding molecular structures and Bader charge analysis (Table 3).

The higher adsorption energy of IM1 on $\text{Co}_6@Au_{32}$ compared to Au_{38} is because the small O1 band of $\text{Co}_6@Au_{32}$ around the Fermi energy is completely in the bonding state whereas that of Au_{38} still has some antibonding characteristics (Figures 5b2 and 6b2). It is mostly due to π back-donation of Au d electrons and the charge transfer between the unoccupied $1\pi^*$ orbital of CO and the Au d states with Au(C1) and Au(C2) changing from negative to positive charge. The main difference between TS1 on these two nanoparticles is the H_2O adsorption site, hcp for $\text{Co}_6@Au_{32}$ and T_2 for Au_{38} , mainly because of the combination of the CO coadsorption and the distance shrinkage between the shell Au atoms in $\text{Co}_6@Au_{32}$. Without the Au distance shrinkage, this

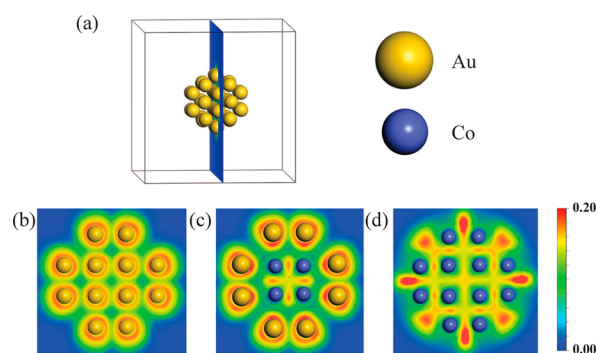


Figure 4. Electron localization function (ELF) diagrams (a) sliced along the (200) plane in the bounding box of (b) Au_{38} , (c) $\text{Co}_6@Au_{32}$, and (d) Co_{38} nanoparticles.

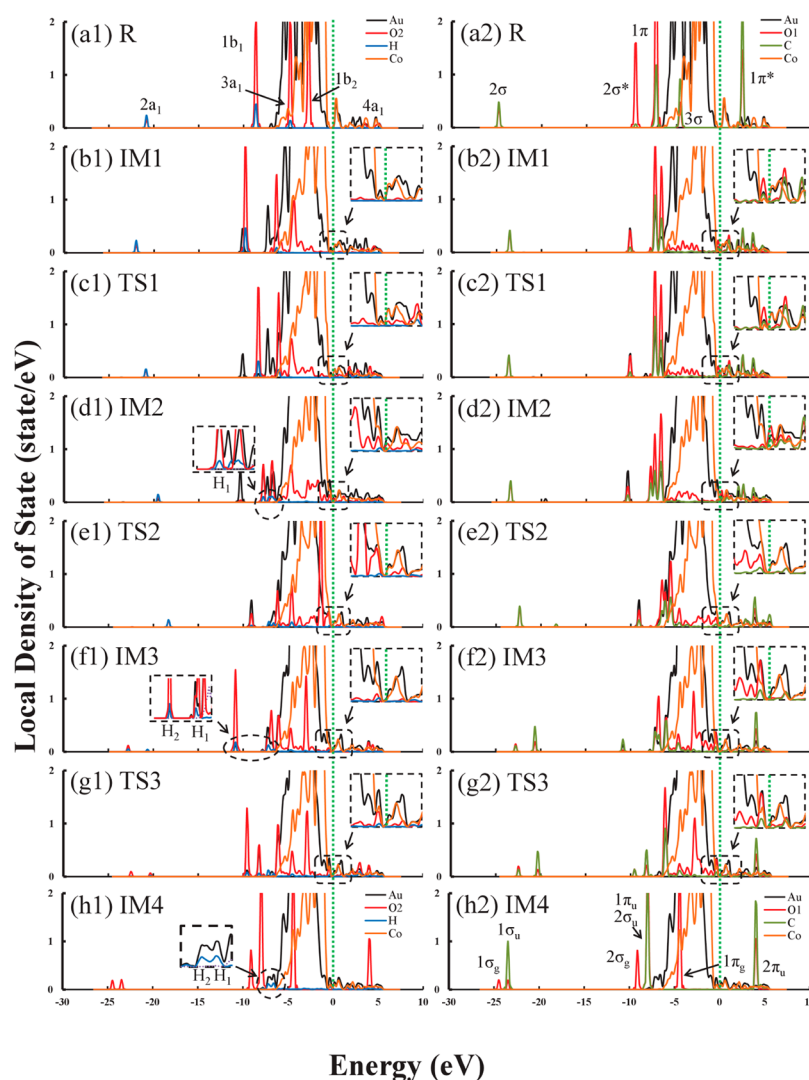


Figure 5. Calculated electronic LDOS of the system projected onto the orbitals for the adsorbed constructs of H₂O (left panel) and CO (right panel) species on Co₆@Au₃₂, as well as the d-projected electron density of the bound Au (black) and Co (purple) atoms. The blue, red, olive green, orange, and black lines represent the LDOS of hydrogen, oxygen, carbon, Co (d band), and Au (d band), respectively. The green dashed line represents the Fermi level.

site on Au₃₈ is still not a stable H₂O adsorption site even with CO coadsorption. Although CO coadsorption plays an important role in the stabilization of H₂O adsorption on an hcp site, the orbitals of CO(ads) between IM1 and TS1 remain almost the same. Therefore the stabilization of H₂O adsorption is through the interaction with the Au atom [Au(C2) in Table 3], which bonds with both CO and H₂O. Because H₂O resides on an hcp site for Co₆@Au₃₂, the TS1 conformation requires the to-be-broken OH bond to be stretched from 0.98 to 1.26 Å toward a B₂ site, which is less than that for Au₃₂ (from 1.00 to 1.35 Å), with H₂O locating at a T₂ site and the dissociating H atom also pointing toward a B₂ site. The shorter stretching bond length is the main reason why the energetic barrier to water dissociation on Co₆@Au₃₂ is smaller than that on Au₃₈.

After the first hydrogen dissociation, H₂O(ads) becomes HO(ads) with one extra unpaired electron in addition the original nonbonding 1b₂ paired electrons, and the adsorption changes into chemisorption. The configuration of IM2 has OH adsorbed on an hcp site and the dissociated H atom (H1 in Table 3) on a B2 site on Co₆@Au₃₂, but the adsorbed OH radical on Au₃₈ resides on a T₂ site. A new peak in the Au₃₈

LDOS (approximately −0.9 eV) indicates the existence of the extra unpaired electron on O2 and stabilization by the metal (Figure 6d1), but this peak is barely noticeable on the Co₆@Au₃₂ LDOS (Figure 5d1). It is because the short Au–Au distance in Co₆@Au₃₂ and the occupation of an hcp site brings OH(ads) close to both Au(C2) (2.46 Å) and H1(ads) (3.32 Å) to allow an interaction with them. The interaction between OH(ads) and Au(C2) causes the 1π orbital of CO splitting and increases the intensity of the O1 antibonding states at the same time. Meanwhile, on Co₆@Au₃₂, the interaction between OH(ads) and H1(ads) reduces the radical characteristics of OH(ads) to cause H1(ads) to still overlap with the O2 orbital and suppress the peak of the unpaired electron in O2 (approximately −0.9 eV) as found for OH(ads) on Au₃₈. These interactions allow OH to adsorb on the original unstable hcp site, but they are also why the reaction of water dissociation on Co₆@Au₃₂ is more endothermic than that on Au₃₈, because the dissociated H atom is adsorbed on a B₂ site, which is less stable than the other sites, such as B₁ and T₁ sites (Table 2).

In TS2, OH(ads) and CO(ads) form a partial bond with each other, and OH(ads) moves upward and away from the

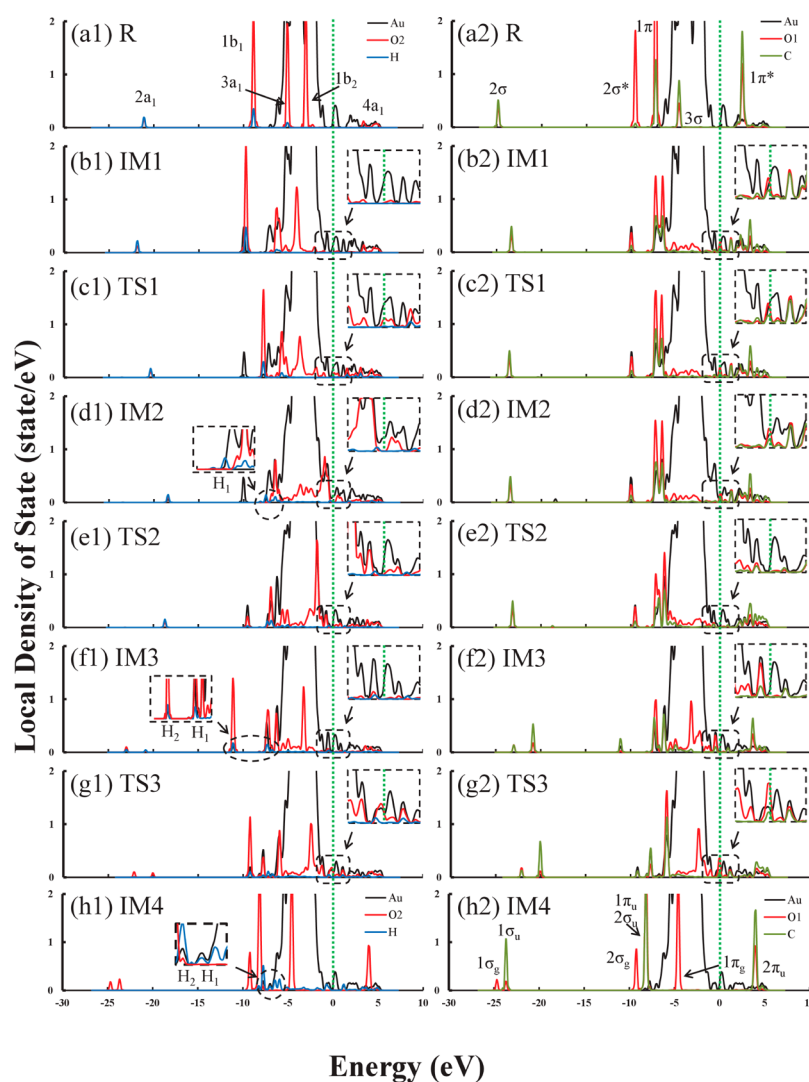


Figure 6. Calculated electronic local densities of states of the system projected on the orbitals for the adsorbed constructs of H₂O (left panel) and CO (right panel) species on Au₃₈, as well as the d-projected electron density of the bound Au (black) atoms. The blue, red, olive green, and black lines represent the LDOS of hydrogen, oxygen, carbon, and Au(d band), respectively. The green dashed line represents the Fermi level.

nanoparticle to make the O₂-related orbitals become sharp, similar to those found in the gas phase (Figures 5e1 and 6e1). The lower energetic barrier of this associated reaction on Co₆@Au₃₂ compared to Au₃₈ is due to the greater π back-donation of Au d electrons on Co₆@Au₃₂, such as that found in IM1. After IM3 is formed, the LDOS patterns of the two panels for the oxygen orbitals become similar, except that O₂ still bonds to H₂ and O₁ has the characteristics of metal back-donation found in both nanoparticles. The main reason for the lower exothermicity in the carboxyl formation reaction on Co₆@Au₃₂ compared to Au₃₈ is mainly because the adsorption energy of the H atom on a B₂ site of Co₆@Au₃₂ is less than that on Au₃₈ (Table 2). Because the dissociated H atoms act as spectators after their dissociation except for the formation reaction of hydrogen molecules (reaction vii), the migration of H₁ to other sites can be considered as the isomerization reaction of IM3. Because reaction heat is a thermodynamic property, the system should be allowed to search the conformation space to reach thermal equilibrium. If H₁ moves to the site with a higher adsorption energy, such as B₁ or T₁, the reaction of carboxyl formation on Co₆@Au₃₂ would become approximately 12 kcal/mol more exothermic than that with H₁ adsorbed on a B₂ site.

Thus, carboxyl formation on Co₆@Au₃₂ would be more exothermic than that on Au₃₈.

In the final hydrogen dissociation reaction, the LDOS of TS3 on Co₆@Au₃₂ resembles that of IM3. Compared with Au₃₈, there are some differences between IM3 and TS3 in terms of LDOS, especially around the Fermi energy. Because of the higher degree of similarity in electronic structures, the energetic barrier of the final hydrogen dissociation on Co₆@Au₃₂ is lower than that on Au₃₈. The greater endothermicity of this hydrogen dissociation on Co₆@Au₃₂ compared to Au₃₈ is due to the adsorption site of the dissociating H atoms, similar to that found in the carboxyl formation reaction.

CONCLUSIONS

We have compared the reaction mechanism of the water–gas shift reaction catalyzed by a Co₆@Au₃₂ nanoparticle against that for a Au₃₈ nanoparticle, as well as the related adsorption configurations and their electronic properties at the DFT level in conjunction with the PAW approach. Our results show that the adsorptions and reactivity of Co₆@Au₃₂ are more similar to those of Au₃₂ than to those of Co₃₂. However, the related energies of all of the WGS chemical species on a Co₆@Au₃₂

nanoparticle are lower than those of the gas-phase reactants with the clean nanoparticle, and therefore, the WGSR on a Co₆@Au₃₂ nanoparticle should be able to proceed under ambient pressure, without the high pressure required for that taking place on a Au₃₈ nanoparticle. The calculated reaction rate constant for the rate-limiting step [H₂O(ads) → H(ads) + OH(ads)] predicts that the WGSR can take place on a Co₆@Au₃₂ nanoparticle with a reasonable reaction rate at low temperature. These advantages are mainly contributed from the core Co atoms, which control not only the geometry of the surface Au atoms but also the electronic structure near the Fermi energy. Accordingly, we predict that the bimetallic Co₆@Au₃₂ nanoparticle has better catalytic activity for the WGSR, as it combines the advantages of the catalytic behavior of Au metal and the better adsorption ability of Co metal.

■ ASSOCIATED CONTENT

■ Supporting Information

Adsorption sites of WGSR-related chemical species on the nanoparticles (Table S1). Isomers of adsorbed CO, H₂O, OH, and H on the Co₆@Au₃₂ nanoparticle and their optimized geometric parameters (Figures S1–S4, respectively). Geometry simulations of intermediates, transition states, and products for the WGSR (Figure S5). The two major reactions related to the redox mechanism for the WGSR (Figure S6). This material is available free of charge via the Internet at <http://pubs.acs.org>.

■ AUTHOR INFORMATION

Corresponding Author

*Tel.: 886-4-22840411. E-mail: feng64@nchu.edu.tw.

Author Contributions

†S.-K.W. and R.-J.L. contributed equally to this work

Notes

The authors declare no competing financial interest.

■ ACKNOWLEDGMENTS

We are grateful to National Center for High-performance Computing, Taiwan, for the computer time and facilities. The National Science Council of Republic of China (NSC 102-2113-M-0005-007) supported this work.

■ REFERENCES

- (1) Haruta, M.; Kobayashi, T.; Sano, H.; Yamada, N. Novel Gold Catalysts for the Oxidation of Carbon Monoxide at a Temperature Far Below 0° C. *Chem. Lett.* **1987**, 405–408.
- (2) Haruta, M.; Daté, M. Advances in the Catalysis of Au Nanoparticles. *Appl. Catal. A: Gen.* **2001**, 222, 427–437.
- (3) Hutchings, G. J. Supported Gold and Gold Palladium Catalysts for Selective Chemical Synthesis. *Catal. Today* **2008**, 138, 9–14.
- (4) McEwan, L.; Julius, M.; Roberts, S.; Fletcher, J. C. A Review of the Use of Gold Catalysts in Selective Hydrogenation Reactions. *Gold Bull.* **2010**, 43, 298–306.
- (5) Haruta, M. Size- and Support-Dependency in the Catalysis of Gold. *Catal. Today* **1997**, 36, 153–166.
- (6) Haruta, M. Catalysis: Gold Rush. *Nature* **2005**, 437, 1098–1099.
- (7) Roldán, A.; González, S.; Ricart, J. M.; Illas, F. Critical Size for O₂ Dissociation by Au Nanoparticles. *ChemPhysChem* **2009**, 10, 348–351.
- (8) Valden, M.; Lai, X.; Goodman, D. W. Onset of Catalytic Activity of Gold Clusters on Titania with the Appearance of Nonmetallic Properties. *Science* **1998**, 281, 1647–1650.
- (9) Zhang, Y.; Cui, X.; Shi, F.; Deng, Y. Nano-Gold Catalysis in Fine Chemical Synthesis. *Chem. Rev.* **2011**, 112, 2467–2505.
- (10) Turner, M.; Golovko, V. B.; Vaughan, O. P.; Abdulkin, P.; Berenguer-Murcia, A.; Tikhov, M. S.; Johnson, B. F.; Lambert, R. M. Selective Oxidation with Dioxide by Gold Nanoparticle Catalysts Derived from 55-Atom Clusters. *Nature* **2008**, 454, 981–983.
- (11) Venugopal, A.; Aluha, J.; Scurrrell, M. S. The Water–Gas Shift Reaction over Au-Based, Bimetallic Catalysts. The Au–M (M = Ag, Bi, Co, Cu, Mn, Ni, Pb, Ru, Sn, Ti) on Iron(III) Oxide System. *Catal. Lett.* **2003**, 90, 1–6.
- (12) Yuan, G.; Lopez, J. L.; Louis, C.; Delannoy, L.; Keane, M. A. Remarkable Hydrodechlorination Activity over Silica Supported Nickel/Gold Catalysts. *Catal. Commun.* **2005**, 6, 555–562.
- (13) Keane, M. A.; Gómez-Quero, S.; Cárdenas-Lizana, F.; Shen, W. Alumina-Supported Ni–Au: Surface Synergistic Effects in Catalytic Hydrodechlorination. *ChemCatChem* **2009**, 1, 270–278.
- (14) Venezia, A.; Liotta, L.; Pantaleo, G.; La Parola, V.; Deganello, G.; Beck, A.; Koppány, Z.; Frey, K.; Horvath, D.; Gucci, L. Activity of SiO₂ Supported Gold-Palladium Catalysts in Co Oxidation. *Appl. Catal. A: Gen.* **2003**, 251, 359–368.
- (15) Bonarowska, M.; Malinowski, A.; Juszczak, W.; Karpiński, Z. Hydrodechlorination of CCl₂F₂ (CFC-12) over Silica-Supported Palladium–Gold Catalysts. *Appl. Catal. B: Environ.* **2001**, 30, 187–193.
- (16) Nutt, M. O.; Heck, K. N.; Alvarez, P.; Wong, M. S. Improved Pd-on-Au Bimetallic Nanoparticle Catalysts for Aqueous-Phase Trichloroethene Hydrodechlorination. *Appl. Catal. B: Environ.* **2006**, 69, 115–125.
- (17) Hurtado-Juan, M.; Yeung, C. M.; Tsang, S. C. A Study of Co-Precipitated Bimetallic Gold Catalysts for Water–Gas Shift Reaction. *Catal. Commun.* **2008**, 9, 1551–1557.
- (18) Yu, Q.; Chen, W.; Li, Y.; Jin, M.; Suo, Z. The Action of Pt in Bimetallic Au–Pt/CeO₂ Catalyst for Water–Gas Shift Reaction. *Catal. Today* **2010**, 158, 324–328.
- (19) Suo, Z.; Ma, C.; Jin, M.; He, T.; An, L. The Active Phase of Au–Pd/Al₂O₃ for Co Oxidation. *Catal. Commun.* **2008**, 9, 2187–2190.
- (20) Suo, Z.; Lv, A.; Lv, H.; Jin, M.; He, T. Influence of Au Promoter on Hydrodesulfurization Activity of Thiophene over Sulfided Au–Ni/SiO₂ Bimetallic Catalysts. *Catal. Commun.* **2009**, 10, 1174–1177.
- (21) Çağlayan, B. S.; Aksoylu, A. E. Water–Gas Shift Activity of Ceria Supported Au–Re Catalysts. *Catal. Commun.* **2011**, 12, 1206–1211.
- (22) Ferrando, R.; Jellinek, J.; Johnston, R. L. Nanoalloys: From Theory to Applications of Alloy Clusters and Nanoparticles. *Chem. Rev.* **2008**, 108, 845–910.
- (23) Schmid, G.; Lehnert, A.; Malm, J. O.; Bovin, J. O. Ligand-Stabilized Bimetallic Colloids Identified by HRTEM and EDX. *Angew. Chem., Int. Ed.* **1991**, 30, 874–876.
- (24) Lee, W.-r.; Kim, M. G.; Choi, J.-r.; Park, J.-I.; Ko, S. J.; Oh, S. J.; Cheon, J. Redox–Transmetalation Process as a Generalized Synthetic Strategy for Core–Shell Magnetic Nanoparticles. *J. Am. Chem. Soc.* **2005**, 127, 16090–16097.
- (25) Jiang, H.-L.; Xu, Q. Recent Progress in Synergistic Catalysis over Heterometallic Nanoparticles. *J. Mater. Chem.* **2011**, 21, 13705–13725.
- (26) Liu, Y.; Fu, Q.; Stephanopoulos, M. Preferential Oxidation of Co in H₂ over CuO–CeO₂ Catalysts. *Catal. Today* **2004**, 93, 241–246.
- (27) Song, C. Fuel Processing for Low-Temperature and High-Temperature Fuel Cells: Challenges and Opportunities for Sustainable Development in the 21st Century. *Catal. Today* **2002**, 77, 17–49.
- (28) Suh, D. J.; Kwak, C.; Kim, J.-H.; Kwon, S. M.; Park, T.-J. Removal of Carbon Monoxide from Hydrogen-Rich Fuels by Selective Low-Temperature Oxidation over Base Metal Added Platinum Catalysts. *J. Power Sources* **2005**, 142, 70–74.
- (29) Liu, P.; Rodriguez, J. A. Water–Gas-Shift Reaction on Metal Nanoparticles and Surfaces. *J. Chem. Phys.* **2007**, 126, 164705.
- (30) Ruettinger, W.; Ilinich, O.; Farrauto, R. J. A New Generation of Water Gas Shift Catalysts for Fuel Cell Applications. *J. Power Sources* **2003**, 118, 61–65.
- (31) Rodriguez, J. A.; Liu, P.; Hrbek, J.; Evans, J.; Pérez, M. Water Gas Shift Reaction on Cu and Au Nanoparticles Supported on

CeO₂(111) and ZnO(0001): Intrinsic Activity and Importance of Support Interactions. *Angew. Chem., Int. Ed.* **2007**, *46*, 1329–1332.

(32) Koryabkina, N.; Phatak, A.; Ruettinger, W.; Farrauto, R.; Ribeiro, F. Determination of Kinetic Parameters for the Water–Gas Shift Reaction on Copper Catalysts under Realistic Conditions for Fuel Cell Applications. *J. Catal.* **2003**, *217*, 233–239.

(33) Geissler, K.; Newson, E.; Vogel, F.; Truong, T.-B.; Hottinger, P.; Wokaun, A. Autothermal Methanol Reforming for Hydrogen Production in Fuel Cell Applications. *Phys. Chem. Chem. Phys.* **2001**, *3*, 289–293.

(34) Cortright, R.; Davda, R.; Dumesic, J. Hydrogen from Catalytic Reforming of Biomass-Derived Hydrocarbons in Liquid Water. *Nature* **2002**, *418*, 964–967.

(35) Choi, Y.; Stenger, H. G. Fuel Cell Grade Hydrogen from Methanol on a Commercial Cu/ZnO/Al₂O₃ Catalyst. *Appl. Catal. B: Environ.* **2002**, *38*, 259–269.

(36) Twigg, M. V.; Spencer, M. S. Deactivation of Supported Copper Metal Catalysts for Hydrogenation Reactions. *Appl. Catal. A: Gen.* **2001**, *212*, 161–174.

(37) Fu, Q.; Saltsburg, H.; Flytzani-Stephanopoulos, M. Active Nonmetallic Au and Pt Species on Ceria-Based Water–Gas Shift Catalysts. *Science* **2003**, *301*, 935–938.

(38) Fu, Q.; Deng, W.; Saltsburg, H.; Flytzani-Stephanopoulos, M. Activity and Stability of Low-Content Gold–Cerium Oxide Catalysts for the Water–Gas Shift Reaction. *Appl. Catal. B: Environ.* **2005**, *56*, 57–68.

(39) Rodriguez, J. A. Gold-Based Catalysts for the Water–Gas Shift Reaction: Active Sites and Reaction Mechanism. *Catal. Today* **2011**, *160*, 3–10.

(40) Burch, R.; Goguet, A.; Meunier, F. C. A Critical Analysis of the Experimental Evidence for and against a Formate Mechanism for High Activity Water–Gas Shift Catalysts. *Appl. Catal. A: Gen.* **2011**, *409*, 3–12.

(41) Mullen, G. M.; Gong, J.; Yan, T.; Pan, M.; Mullins, C. B. The Effects of Adsorbed Water on Gold Catalysis and Surface Chemistry. *Top. Catal.* **2013**, *56*, 1499–1511.

(42) Burch, R. Gold Catalysts for Pure Hydrogen Production in the Water–Gas Shift Reaction: Activity, Structure and Reaction Mechanism. *Phys. Chem. Chem. Phys.* **2006**, *8*, 5483–5500.

(43) Kalamaras, C. M.; Panagiotopoulou, P.; Kondarides, D. I.; Efstathiou, A. M. Kinetic and Mechanistic Studies of the Water–Gas Shift Reaction on Pt/TiO₂ Catalyst. *J. Catal.* **2009**, *264*, 117–129.

(44) Kalamaras, C. M.; Amerikanou, S.; Efstathiou, A. M. “Redox” vs “Associative Formate with –OH Group Regeneration” WGS Reaction Mechanism on Pt/CeO₂: Effect of Platinum Particle Size. *J. Catal.* **2011**, *279*, 287–300.

(45) Bunluesin, T.; Gorte, R.; Graham, G. Studies of the Water–Gas-Shift Reaction on Ceria-Supported Pt, Pd, and Rh: Implications for Oxygen-Storage Properties. *Appl. Catal. B: Environ.* **1998**, *15*, 107–114.

(46) Gorte, R.; Zhao, S. Studies of the Water–Gas-Shift Reaction with Ceria-Supported Precious Metals. *Catal. Today* **2005**, *104*, 18–24.

(47) Li, Y.; Fu, Q.; Flytzani-Stephanopoulos, M. Low-Temperature Water–Gas Shift Reaction over Cu- and Ni-Loaded Cerium Oxide Catalysts. *Appl. Catal. B: Environ.* **2000**, *27*, 179–191.

(48) Jacobs, G.; Graham, U. M.; Chenu, E.; Patterson, P. M.; Dozier, A.; Davis, B. H. Low-Temperature Water–Gas Shift: Impact of Pt Promoter Loading on the Partial Reduction of Ceria and Consequences for Catalyst Design. *J. Catal.* **2005**, *229*, 499–512.

(49) Jacobs, G.; Williams, L.; Graham, U.; Sparks, D.; Davis, B. H. Low-Temperature Water–Gas Shift: In-Situ DRIFTS–Reaction Study of a Pt/CeO₂ Catalyst for Fuel Cell Reformer Applications. *J. Phys. Chem. B* **2003**, *107*, 10398–10404.

(50) Kalamaras, C. M.; Gonzalez, I. D.; Navarro, R. M.; Fierro, J. L. G.; Efstathiou, A. M. Effects of Reaction Temperature and Support Composition on the Mechanism of Water–Gas Shift Reaction over Supported-Pt Catalysts. *J. Phys. Chem. C* **2011**, *115*, 11595–11610.

(51) Kim, C. H.; Thompson, L. T. Deactivation of Au/CeO_x Water Gas Shift Catalysts. *J. Catal.* **2005**, *230*, 66–74.

(52) Karpenko, A.; Leppelt, R.; Cai, J.; Plzak, V.; Chuvilin, A.; Kaiser, U.; Behm, R. Deactivation of a Au/CeO₂ Catalyst during the Low-Temperature Water–Gas Shift Reaction and Its Reactivation: A Combined TEM, XRD, XPS, DRIFTS, and Activity Study. *J. Catal.* **2007**, *250*, 139–150.

(53) Denkwitz, Y.; Karpenko, A.; Plzak, V.; Leppelt, R.; Schumacher, B.; Behm, R. Influence of CO₂ and H₂ on the Low-Temperature Water–Gas Shift Reaction on Au/CeO₂ Catalysts in Idealized and Realistic Reformate. *J. Catal.* **2007**, *246*, 74–90.

(54) Abd El-Moemen, A.; Karpenko, A.; Denkwitz, Y.; Behm, R. Activity, Stability and Deactivation Behavior of Au/CeO₂ Catalysts in the Water Gas Shift Reaction at Increased Reaction Temperature (300° C). *J. Power Sources* **2009**, *190*, 64–75.

(55) Lin, R.-J.; Chen, H.-L.; Ju, S.-P.; Li, F.-Y.; Chen, H.-T. Quantum-Chemical Calculations on the Mechanism of the Water–Gas Shift Reaction on Nanosized Gold Cluster. *J. Phys. Chem. C* **2012**, *116*, 336–342.

(56) Chen, H.-L.; Su, C.-H.; Chen, H.-T. Catalytic Co Oxidation by Au–Pd Core–Shell Nanoparticles: A First-Principles Study. *Chem. Phys. Lett.* **2012**, *536*, 100–103.

(57) Ma, W.; Chen, F. Co Oxidation on Cu-Doped Ag Clusters. *Theor. Chem. Acc.* **2013**, *132*, 1–6.

(58) Li, H.-J.; Ho, J.-J. Theoretical Calculations on the Oxidation of CO on Au₅₅, Ag₁₃Au₄₂, Au₁₃Ag₄₂, and Ag₅₅ Clusters of Nanometer Size. *J. Phys. Chem. C* **2012**, *116*, 13196–13201.

(59) Huang, S.-C.; Lin, C.-H.; Wang, J.-H. Trends of Water Gas Shift Reaction on Close-Packed Transition Metal Surfaces. *J. Phys. Chem. C* **2010**, *114*, 9826–9834.

(60) Bao, Y.; Calderon, H.; Krishnan, K. M. Synthesis and Characterization of Magnetic-Optical Co–Au Core–Shell Nanoparticles. *J. Phys. Chem. C* **2007**, *111*, 1941–1944.

(61) Robinson, I.; Tung, L. D.; Maenosono, S.; Wälti, C.; Thanh, N. T. Synthesis of Core–Shell Gold Coated Magnetic Nanoparticles and Their Interaction with Thiolated DNA. *Nanoscale* **2010**, *2*, 2624–2630.

(62) Lu, Y.; Zhao, Y.; Yu, L.; Dong, L.; Shi, C.; Hu, M.-J.; Xu, Y.-J.; Wen, L.-P.; Yu, S.-H. Hydrophilic Co@Au Yolk/Shell Nanospheres: Synthesis, Assembly, and Application to Gene Delivery. *Adv. Mater.* **2010**, *22*, 1407–1411.

(63) Mandal, S.; Krishnan, K. M. Co_{core}Au_{shell} Nanoparticles: Evolution of Magnetic Properties in the Displacement Reaction. *J. Mater. Chem.* **2007**, *17*, 372–376.

(64) Zhang, H.; Okuni, J.; Toshima, N. One-Pot Synthesis of Ag–Au Bimetallic Nanoparticles with Au Shell and Their High Catalytic Activity for Aerobic Glucose Oxidation. *J. Colloid Interface Sci.* **2011**, *354*, 131–138.

(65) Enache, D. I.; Edwards, J. K.; Landon, P.; Solsona-Espriu, B.; Carley, A. F.; Herzing, A. A.; Watanabe, M.; Kiely, C. J.; Knight, D. W.; Hutchings, G. J. Solvent-Free Oxidation of Primary Alcohols to Aldehydes Using Au–Pd/TiO₂ Catalysts. *Science* **2006**, *311*, 362–365.

(66) Yang, X.; Cheng, F.; Tao, Z.; Chen, J. Hydrolytic Dehydrogenation of Ammonia Borane Catalyzed by Carbon Supported Co Core–Pt Shell Nanoparticles. *J. Power Sources* **2011**, *196*, 2785–2789.

(67) van Steen, E.; Claeys, M.; Dry, M. E.; van de Loosdrecht, J.; Viljoen, E. L.; Visagie, J. L. Stability of Nanocrystals: Thermodynamic Analysis of Oxidation and Re-Reduction of Cobalt in Water/Hydrogen Mixtures. *J. Phys. Chem. B* **2005**, *109*, 3575–3577.

(68) Tsakoumis, N. E.; Rønning, M.; Borg, Ø.; Rytter, E.; Holmen, A. Deactivation of Cobalt Based Fischer–Tropsch Catalysts: A Review. *Catal. Today* **2010**, *154*, 162–182.

(69) Van Berge, P.; Van de Loosdrecht, J.; Barradas, S.; Van der Kraan, A. Oxidation of Cobalt Based Fischer–Tropsch Catalysts as a Deactivation Mechanism. *Catal. Today* **2000**, *58*, 321–334.

(70) Ban, Z.; O'Connor, C. A Novel Synthesis of Co@Au Nanoparticles and Characterization. In *NSTI-Nanotech 2004*; CRC Press: Boca Raton, FL, 2004; Vol. 3, pp 320–322.

- (71) Kresse, G.; Furthmüller, J. Efficiency of Ab-Initio Total Energy Calculations for Metals and Semiconductors Using a Plane-Wave Basis Set. *Comput. Mater. Sci.* **1996**, *6*, 15–50.
- (72) Kresse, G.; Hafner, J. Ab Initio Molecular Dynamics for Liquid Metals. *Phys. Rev. B* **1993**, *47*, 558.
- (73) Kresse, G.; Hafner, J. Ab Initio Molecular-Dynamics Simulation of the Liquid-Metal–Amorphous-Semiconductor Transition in Germanium. *Phys. Rev. B* **1994**, *49*, 14251.
- (74) Kresse, G.; Hafner, J. Norm-Conserving and Ultrasoft Pseudopotentials for First-Row and Transition Elements. *J. Phys.: Condens. Matter* **1994**, *6*, 8245.
- (75) Kresse, G.; Furthmüller, J. Efficient Iterative Schemes for ab Initio Total-Energy Calculations Using a Plane-Wave Basis Set. *Phys. Rev. B* **1996**, *54*, 11169.
- (76) Hohenberg, P.; Kohn, W. Inhomogeneous Electron Gas. *Phys. Rev.* **1964**, *136*, B864.
- (77) Perdew, J. P.; Burke, K.; Ernzerhof, M. Generalized Gradient Approximation Made Simple. *Phys. Rev. Lett.* **1996**, *77*, 3865.
- (78) Perdew, J. P.; Wang, Y. Accurate and Simple Analytic Representation of the Electron-Gas Correlation Energy. *Phys. Rev. B* **1992**, *45*, 13244.
- (79) Bader, R. F. *Atom in Molecules: A Quantum Theory*; International Series of Monographs in Chemistry; Oxford University Press: Oxford, U.K., 1990.
- (80) Bader, R.; Beddall, P. Virial Field Relationship for Molecular Charge Distributions and the Spatial Partitioning of Molecular Properties. *J. Chem. Phys.* **1972**, *56*, 3320.
- (81) Henkelman, G.; Uberuaga, B. P.; Jónsson, H. A Climbing Image Nudged Elastic Band Method for Finding Saddle Points and Minimum Energy Paths. *J. Chem. Phys.* **2000**, *113*, 9901.
- (82) Mills, G.; Jónsson, H.; Schenter, G. K. Reversible Work Transition State Theory: Application to Dissociative Adsorption of Hydrogen. *Surf. Sci.* **1995**, *324*, 305–337.
- (83) Henkelman, G.; Arnaldsson, A.; Jónsson, H. A Fast and Robust Algorithm for Bader Decomposition of Charge Density. *Comput. Mater. Sci.* **2006**, *36*, 354–360.
- (84) Gershinsky, G.; Pollak, E. Quantum Harmonic Transition State Theory—Application to Isomerization of Stilbene in Liquid Ethane. *J. Chem. Phys.* **1998**, *108*, 2756.
- (85) Garzón, I.; Michaelian, K.; Beltrán, M.; Posada-Amarillas, A.; Ordejón, P.; Artacho, E.; Sánchez-Portal, D.; Soler, J. Lowest Energy Structures of Gold Nanoclusters. *Phys. Rev. Lett.* **1998**, *81*, 1600.
- (86) Rodríguez-López, J.; Aguilera-Granja, F.; Michaelian, K.; Vega, A. Structure and Magnetism of Cobalt Clusters. *Phys. Rev. B* **2003**, *67*, 174413.
- (87) Wang, J.; Bai, J.; Jellinek, J.; Zeng, X. C. Gold-Coated Transition-Metal Anion $[\text{Mn}_{13}@\text{Au}_{20}]^-$ with Ultrahigh Magnetic Moment. *J. Am. Chem. Soc.* **2007**, *129*, 4110–4111.
- (88) Lide, D. R., Ed. *CRC Handbook of Physics and Chemistry*, 88th ed.; CRC Press: Boca Raton, FL, 2003.
- (89) Liu, P.; Rodríguez, J. A. Water–Gas-Shift Reaction on Metal Nanoparticles and Surfaces. *J. Chem. Phys.* **2007**, *126*, 164705.
- (90) Rodríguez, J. A.; Liu, P.; Hrbek, J.; Evans, J.; Pérez, M. Water Gas Shift Reaction on Cu and Au Nanoparticles Supported on $\text{CeO}_2(111)$ and $\text{ZnO}(0001)$: Intrinsic Activity and Importance of Support Interactions. *Angew. Chem., Int. Ed.* **2007**, *46*, 1329–1332.
- (91) Gokhale, A. A.; Dumesic, J. A.; Mavrikakis, M. On the Mechanism of Low-Temperature Water Gas Shift Reaction on Copper. *J. Am. Chem. Soc.* **2008**, *130*, 1402–1414.
- (92) Brønsted, J. N. Acid and Basic Catalysis. *Chem. Rev.* **1928**, *5*, 231–338.
- (93) Evans, M. G.; Polanyi, M. Inertia and Driving Force of Chemical Reactions. *Trans. Faraday Soc.* **1938**, *34*, 11–24.
- (94) Dahl, S.; Logadottir, A.; Jacobsen, C. J.; Nørskov, J. K. Electronic Factors in Catalysis: The Volcano Curve and the Effect of Promotion in Catalytic Ammonia Synthesis. *Appl. Catal. A: Gen.* **2001**, *222*, 19–29.
- (95) Loffreda, D.; Delbecq, F.; Vigné, F.; Sautet, P. Fast Prediction of Selectivity in Heterogeneous Catalysis from Extended Brønsted–Evans–Polanyi Relations: A Theoretical Insight. *Angew. Chem., Int. Ed.* **2009**, *48*, 8978–8980.
- (96) Wang, S.; Temel, B.; Shen, J.; Jones, G.; Grabow, L. C.; Studt, F.; Bligaard, T.; Abild-Pedersen, F.; Christensen, C. H.; Nørskov, J. K. Universal Brønsted–Evans–Polanyi Relations for C–C, C–O, C–N, N–O, N–N, and O–O Dissociation Reactions. *Catal. Lett.* **2011**, *141*, 370–373.
- (97) Forrey, R.; Guvelioglu, G.; Ma, P.; He, X.; Cheng, H. Rate Constants for Dissociative Chemisorption of Hydrogen Molecules on Copper Clusters. *Phys. Rev. B* **2006**, *73*, 155437.
- (98) Hammer, B.; Nørskov, J. K. Theoretical Surface Science and Catalysis—Calculations and Concepts. *Adv. Catal.* **2000**, *45*, 71–129.